1 # Magnesium isotope evidence for enhanced crustal reworking

2 # in lowermost Cambrian sedimentary rocks (Kazakhstan)

3

4 **Jessica A. Stammeier[1,2]*, Dorothee Hippler[1], Oliver Nebel[3], and Martin Dietzel [1]**

5 *[1] Institute of Applied Geosciences, Graz University of Technology, Rechbauerstraße 12, 8010*

6 *Graz, Austria*

7 *[2] GFZ German Research Centre for Geosciences, Telegrafenberg, 14473 Potsdam, Germany*

8 *[3] School of Earth, Atmosphere and Environment, Monash University, Clayton VIC 3800,*

9 *Australia*

10 *corresponding author email: j.stammeier@web.de

11

12

13 **ABSTRACT**

14 The transition from the Proterozoic to the Phanerozoic Eon was accompanied by the rise

15 of metazoan life, a key and unique biogeochemical milestone in Earth's history. Concomitant

16 continental re-organization and collision were associated with enhanced continental reworking

17 and changes in global ocean currents with profound impacts on continental weathering rates,

18 riverine run-off and associated changes in the ocean nutrient budget. The causal relationship

19 between the geological re-organisation of continents and the biologic evolution of marine life,

20 however, remains elusive. In this study, we investigate phosphatic shallow-water sedimentary

21 successions from Kazakhstan, which host key marker horizons from the Precambrian-Cambrian

22 (Pc-C) boundary. We show that a rapid change (ca. 3 Myr) towards heavier stable Mg isotope

23 compositions of the phosphatic sedimentary deposits in Kazakhstan, which we consider

24 representative for contemporaneous ocean chemistry, co-varies with changes in radiogenic Sr

25 isotope signatures. . We propose that ocean chemistry at the Pc-C boundary, represented through

26 this co-variation, was strongly affected by continental re-organization and associated weathering,

27 which, in analogy, would have affected ocean nutrient levels. A rapid reversal of isotope

28 compositions towards signatures similar to those prior to the isotope excursion likely reflects the

29 fading influence of weathering and a buffering of water-rock interactions during oceanic

30 spreading. We conclude, that based on the positive, coupled $^{87}Sr/^{86}Sr$- $\delta^{26}Mg$ isotope spike in

31 ocean water chemistry, a link between Gondwana re-organization at the Pc-C boundary and the

32 marked change in marine fauna thus seems plausible.

33

1. Introduction

35 The Precambrian-Cambrian (Pc-C) transition has long been recognized as a critical point

36 in Earth´s history, marking the rise of metazoan life following the first aquatic mass extinction of

37 the Ediacaran fauna at ca. 541 Ma (e.g., Darroch et al., 2018; Laflamme et al., 2013). Most

38 prominent environmental and geological factors associated with this change in the biosphere are

39 (I) oceanic and atmospheric oxygenation; (II) crustal reworking (continental weathering, erosion)

40 and high nutrient supply into the marine realm with subsequent chert and phosphate deposition;

41 (III) perturbation to nutrient cycling; and (IV) the re-assemblage of continental masses (e.g.,

42 Zhang et al., 2014, Smith and Harper, 2013, and references therein). Despite decades of research,

43 causal relationships between the biologic, ecologic and geologic features and respective timing

44 of oxygenation relative to the Pc-C transition remain controversial, and an individual trigger

45   initiating the secular change from Ediacaran to Cambrian fauna is yet to be identified (Fox,

46   2016).

47   Increasing $^{87}Sr/^{86}Sr$ in seawater during the late Neoproterozoic has been linked to the

48   exposure of radiogenic, cratonic crust during the break-up of Rodinia (Halverson et al., 2009)

49   and enhanced weathering rates and continental run-off (Derry et al., 1994). A sharp, positive

50   excursion in Sr isotopes at the Pc-C transition has been suggested to reflect a higher influx of

51   evolved, crustal material (Burns et al., 1994), which was subsequently counterbalanced by

52   increased hydrothermal activity. More recent studies, which also recognized a positive excursion

53   (e.g., Li et al., 2013), however, dismissed very radiogenic Sr isotopes as poor preservation and/or

54   diagenetic alteration, and with this their environmental significance. Yet, this extremely positive

55   excursion in radiogenic Sr isotopes can be observed at different locations worldwide (Brasier et

56   al., 1996; Derry et al., 1994; Halverson et al., 2010; Nicholas, 1996; Sawaki et al., 2008). A

57   contemporaneous positive $^{87}Sr/^{86}Sr$ peak has recently been recorded in early Cambrian carbonate

58   and phosphorite sections of the Malyi Karatau, Kazakhstan (Stammeier et al., 2019a), rendering

59   these sections a suitable archive for further investigations regarding the potential causes of the

60   excursion. The sedimentary rocks were deposited during the Pc-C episode in a former shallow-

61   water basin. They likely represent global ocean evolution and have been interpreted to reflect

62   enhanced crustal reworking, i.e., continental weathering and erosion (Stammeier et al., 2019a).

63   This temporal relationship supports a scenario in which changes in biodiversity were linked to

64   geodynamic responses of plate re-organization. Whilst detailed relations are far more complex,

65   this would generally link the evolution of Cambrian biota to passive margin dynamics.

66   A test for the degree and impact of continental weathering to ocean chemistry is

67   potentially captured in distinct stable isotope signatures of authigenic, abiotic shallow-water

68   sedimentary rocks. Magnesium is a major component during chemical weathering and abiotic

69   carbonate precipitation (Berner et al., 1983). Thus, the Mg isotope composition of seawater is

70   largely influenced by flux imbalances between weathering and carbonate precipitation processes;

71   detailed knowledge of these influences has been used to trace changes in the weathering regime

72   before (e.g., Kasemann et al., 2014; Pogge von Strandmann et al., 2014; Pokrovsky et al., 2011;

73   Tipper et al., 2006a, 2006b; Wimpenny et al., 2014).

74   Herein, we present new Mg isotope data for the Kazakhstan section and compare them

75   with previously reported radiogenic Sr isotope variations (Stammeier et al., 2019a). Combined

76   with published global $^{87}Sr/^{86}Sr$ seawater signatures, we evaluate the consequences of differences

77   in Mg and Sr isotopes in a dynamic time-dependent state model and aim to validate these results

78   with plausible causes for seawater excursions in light of enhanced weathering rates, carbonate

79   precipitation and hydrothermal activity.

80

81   **2. Sample description**

82   The Koksu section and the herein investigated samples have previously been described in

83   detail by Stammeier et al., (2019a) in terms of petrography and geochemistry. A summary of the

84   investigated sample material and micrographs can be found in Appendix A. Briefly, the section

85   (43° 39' 13.0'' N, 69° 38' 11.0'' E) is located in the Malyi Karatau mountain range, South

86   Kazakhstan and comprises sedimentary rocks of the Fortunian and Stage 2 of the lower

87   Cambrian (541 - 521 Ma, Figs.1 and 2). The 50-m-long profile crops out along an abandoned

88   exploration trench comprising a consecutive sequence of the Chulaktau Formation (Fm.), which

89   consists in its lower part mainly of cherts and phosphorites. The investigated samples belong to

90   the two lowermost members of the Chulaktau Fm., (1) the Aksai Chert, bedded, dark-colored

91   cherts with variable dolomitic and phosphatic content, and (2) the Lower Phosphorite, cross-

92   bedded, granular phosphorites with a calcite and/or dolomite matrix. Internal structure, element

93   and isotope systematics classified these rocks as near primary sedimentary rocks (see detailed

94   discussion in Stammeier et al., 2019a).

95

96   **3. Methodology**

97   To evaluate the effect of our leaching procedure a two-step acid leaching approach, using

98   0.05 mol l^{-1} and 3 mol l^{-1} HNO_3, respectively, was employed in a pre-study. These leaching

99   experiments were conducted on two selected samples with different matrix (dolomite vs. calcite)

100   and texture (phos-grainstone (KO 10) vs. phos-rudstone (KO 13)). From each sample, ca. 20 mg

101   powder was microdrilled. The powders were leached in 0.05 mol l^{-1} HNO_3, rinsed with Milli-Q®

102   three times, and dried down. Each dried sample was then leached in 3 mol l^{-1} HNO_3 and

103   subsequently rinsed with Milli-Q® three times. Each leachate, incl. the Milli-Q®-rinse, was

104   decanted, evaporated and then digested in 2 mol l^{-1} HNO_3 for Mg separation. The results are

105   depicted in Figure 3 and reveal identical Mg isotope composition for both acid leachates within a

106   reproducibility of $\pm$ 0.10 ‰ for $\delta^{26}Mg$, expressed as 2 S.D. Based on these results, bulk sample

107   powders were leached in 3 mol l^{-1} HNO_3 for 24h at 70°C, capturing both carbonate fluorapatite

108   (CFA) and carbonate phases (calcite and dolomite). This acid-soluble fraction was used for all

109   consecutive elemental analysis and separations. The Mg fraction was purified with a two-step ion

110   exchange chemistry using BioRad AG50-X12 resin and HNO_3 and HCl as eluent agents (after

111   Pogge von Strandmann, 2008; Wombacher et al., 2009). For method and analytical details please

112   compare (Stammeier et al., 2019b). In brief, Ca was eliminated by passing the samples over the

113   columns using 15 ml of 2 mol l^{-1} HNO_3. All other interfering cations were eluted using 30 ml of

114   0.4 mol l^{-1} HCl. Magnesium was then collected in 5 ml 5 mol l^{-1} HCl. Yields and interferences

115   were routinely tested to ensure a complete recovery of Mg. Measurements were performed on a

116   Nu Plasma II MC-ICP-MS (Nu Instruments, Wrexham, UK) at the NAWI Graz, Central Lab for

117   Water, Minerals and Rocks (NAWI Graz Geocenter, Austria). Analyses were typically

118   performed in wet plasma with a sensitivity of ca. 12.5 V for 500 µg ml^{-1} on ^{24}Mg using a 0.1

119   ml/min nebulizer. Data acquisition consisted of 1 block with 25 cycles with an integration time

120   of 5 seconds each. The background was determined by 10 seconds integration time at half

121   masses, i.e., with 0.5 amu offset before each block (cf. Aciego et al., 2009; Jackson and Attalla,

122   2010). Measurements were performed with standard-sample-bracketing (SSB) and are reported

123   in the δ-notation as per mil (‰) deviation relative to DSM3. Concentration of reference materials

124   and samples was adjusted to match within 10%. Repeated measurements of reference material

125   Cambridge-1 (Cam-1, Romil Ltd., Cambridge, UK) yielded -2.64 ± 0.10 ‰ for δ^{26}Mg and -1.36

126   ± 0.04 ‰ for δ^{25}Mg (2 SD, n=23), identical to previously reported values by Mavromatis et al.

127   (2014). Reproducibility of the total procedure was tested using JDo-1, which yielded -2.47 ±

128   0.10 ‰ for δ^{26}Mg and -1.30 ± 0.02 ‰ for δ^{25}Mg (2 SD, n=3). Procedural blank was typically

129   below 50 ng l^{-1} for Mg and thus negligible.

130

131   **4. Results**

132   **4.1. Stable Mg isotope record throughout the sedimentary profile**

133   Magnesium isotope analyses of the acid-soluble fraction yield δ^{26}Mg values ranging from

134   -2.3 ‰ to 0.5 ‰ (relative to the DSM3 reference material) with a mean of -1.0 ± 0.2 ‰ (2 SE,

135   n= 13). The observed temporal trend of decreasing δ^{26}Mg towards younger samples appears to

136   correlate considerably with previously investigated ^{87}Sr/^{86}Sr values (Fig. 2, Appendix A;

137   Stammeier et al., 2019a). However, a plot of $\delta^{26}Mg$ vs. $^{87}Sr/^{86}Sr$ displays no correlation, with an

138    $R^2 < 0.1$ (Fig. 4, inset A), indicating that these isotopes may not reflect the same genetic process.

139   Yet, the evident temporal evolution in both proxies indicates a common overall trigger in isotope

140   variability that possibly affects both elements differently. Moreover, $\delta^{26}Mg$ values are anti-

141   correlated with $\delta^{13}C_{carb}$ and $\delta^{18}O_{carb}$ (Fig. 2), the latter reflecting ambient environmental and

142   depositional conditions. To the authors' knowledge, these $\delta^{26}Mg$ are the highest reported values

143   in dolomites to date. Geske et al., (2015) investigated suites of dolomites from different

144   environmental settings and reported a considerably large range of $\delta^{26}Mg$ values ranging from -

145   2.49 ‰ to -0.45 ‰, where the highest values were found in non-marine and hydrothermal

146   settings. Positive $\delta^{26}Mg$ values, as found in two samples from the present study, are typically a

147   feature only exhibited by silicates (Farkaš et al., 2013; Higgins and Schrag, 2010). In general,

148    $\delta^{26}Mg$ in dolomite mainly reflects the composition of the source fluid and is only insignificantly

149   altered during diagenetic alteration or low grade metamorphism (Geske et al., 2015b, 2015a).

150   Accordingly, the sediments studied here have most likely been deposited in a shallow-marine

151   environment (Stammeier et al., 2019a), and likely reflect changing $\delta^{26}Mg$ source composition.

152   As a result, the correlation between $\delta^{26}Mg$ and $\delta^{18}O$ values of these sediments from Kazakhstan

153   is insignificant with an $R^2 < 0.1$ (Fig. 4, inset B).

154   **4.2. $\delta^{26}Mg$ and $^{87}Sr/^{86}Sr$ ocean budgets in a time-dependent dynamic state model**

155   The significance and meaning of both, stable Mg and radiogenic Sr isotopes can be tested

156   with a mass balance model that equates elemental and isotopic input and output fluxes for the

157   past ocean basin (Tipper et al., 2006b). To reconstruct the radiogenic Sr and Mg isotope

158   evolution during the Pc-C transition, we used a time-dependent dynamic state model based on

159   the equation

160
$$\frac{dNR_{sw}}{dt} = \sum F_{in} R_{in} - \sum F_{out} R_{out} \qquad (1)$$

161   describing the isotopic evolution R_{SW}, where SW denotes seawater, of reservoir N as a

162 function of the fluxes F in and out of the reservoir with the attributed isotope composition R

163 (e.g., Richter et al., 1992).

164   Considering the residence time (τ) in Myr as

165
$$\tau = N_{(t)}/\Sigma F_{in} \qquad (2)$$

166 the time-dependent evolution can be described by

167
$$R_{sw}(t) = R_{sw-SX} - (R_{sw-SX} - R_{sw-t0})e^{(\Delta t)/\tau} \qquad (3)$$

168   (detailed mathematical derivation is given by Hodell et al., 1989), where X denotes the

169 respective steady state conditions for Mg or Sr (see below). Note that $N_{(t)}$ includes changes of the

170 reservoir size in response to changing fluxes.

171   As a first order approximation, the main source to the Mg budget in seawater is riverine

172 influx (F_R), which is counterbalanced by output via carbonate precipitation from seawater (F_C)

173 and hydrothermal removal through interaction of sea water with mid ocean ridge basalts

174 (MORB; F_H). Here, we can assume that $R_{SW} = R_H$ as Mg isotope fractionation through

175 hydrothermal removal is generally negligible (de Villiers et al., 2005; Pogge von Strandmann et

176 al., 2014). This yields the equation for steady state conditions (R_{SW-S}) for Mg in seawater:

177
$$R_{sw-SMg} = \frac{F_R R_R - F_C R_C}{F_R - F_C} . \qquad (4)$$

178   For the Sr isotope ocean budget, carbonate precipitation constitutes the main sink of Sr

179 (Palmer and Edmond, 1989). Radiogenic Sr isotopes do not fractionate during carbonate

180 precipitation, thus we can set $R_{sw} = R_{out}$. The remaining fluxes into the ocean are mainly of

181 riverine (F_R), hydrothermal (F_H) and diagenetic (F_D) origin. Assuming $dR_{sw}/dt = 0$, Equation (1)

182 yields the steady state equation (R_{SW-SSr}) for Sr in seawater:

183
$$R_{sw-SSr} = \frac{F_R R_R + F_H R_H + F_D R_D}{F_R + F_H + F_D}.$$
(5)

184   The model calculates the Mg and Sr isotope composition of the ocean in iterative steps of

185 1 Myr covering the time from mid-Ediacaran (560 Ma) to the Early Cambrian (521 Ma). This

186 was done in two general approaches: (i) using the steady state conditions to evaluate the

187 responses of the reservoir to steady changes; and (ii) applying a dynamic change of parameters,

188 in order to achieve a 'best fit' of the observed data (Figs. 5 and 6).

189

190   **4.2.1.**   **δ^{26}Mg in seawater and carbonates**

191   Experimental studies have shown that dolomite formation (assuming ideal stoichiometry)

192 constitutes the majority of the Mg sink through carbonate removal, and can be estimated to

193 account for Δ^{26}Mg$_{Dol-SW}$ of ca. -1.7 to -2.7‰ (Geske et al., 2015b; Higgins and Schrag, 2010; Li

194 et al., 2015). Hence Mg isotopes in carbonates can only indirectly reflect seawater composition.

195 Thus, δ^{26}Mg of carbonates was calculated for each iterative step as a function of changing

196 seawater composition. The Δ^{26}Mg$_{Dol-SW}$ was kept constant throughout the model using an

197 average value of Δ^{26}Mg$_{Dol-SW}$ = 2.0 ‰. For simplification we consider this isotope fractionation

198 factor to be a representative estimate for global carbonate removal, given the diversity of settings

199 and parameters, e.g., temperature. The isotope fractionation factor between Mg calcite

200 (limestone) and precipitation solution would be larger with Δ^{26}Mg$_{CC-SW}$ of ca. -3.6 ‰ (Fantle and

201 Higgins, 2014). However, given stoichiometry, this has a smaller impact on Mg mass balance.

202 Assuming a greater proportion of Mg-calcite on overall carbonate removal, the removal of light

203 isotopes during times of increased carbonate precipitation would be enhanced, producing a Mg$_{SW}$

204 evolution with higher amplitudes (Fig. 7). δ^{26}Mg of the riverine influx was set to R$_R$ = -0.5 ‰,

205 representing silicate dominated weathering and kept constant (see Section 5.1; Tipper et al.,

206   2006; Wimpenny et al., 2014). Tipper et al., (2006) suggest that during times of increased

207   dolomitization, $\delta^{26}Mg_{SW}$ could have been up to 1.5‰ heavier than present-day seawater.

208   Accordingly, initial $\delta^{26}Mg_{SW}$ was set to +0.8 ‰.

209   For this seawater $\delta^{26}Mg$ model, the riverine influx F_R and removal through carbonate

210   precipitation F_C were changed as a function of time, as continental weathering and carbonate

211   deposition were likely the strongest influences on $\delta^{26}Mg_{SW}$ at that time. With the condition that

212    $\Sigma F_{in} = \Sigma F_{out}$, F_H is defined by the difference of F_R-F_C. The initial values are reported in Table 1.

213   The initial magnitude of riverine Mg input (F_R) is adapted from Wilkinson and Algeo (1989) and

214   removed from the ocean by F_H and F_C in equal proportions.

215   For Mg, leaving all fluxes and isotope ratios unchanged, R_{SW} initially decreases and

216   reaches steady state conditions after ca 10 Myr at 549 Ma, converging a R_{SW} = 0 ‰ and thus R_C

217   of -2.0 ‰ (Fig. 5, inset A). Although, these initial 10 Myr broadly match the magnitude of the

218   observed data from Pokrovsky et al., (2011), the observed Mg values in this study suggest much

219   heavier R_{SW} thereafter. Shifting R_{SW} towards lighter values is most easily achieved by decreasing

220   carbonate removal F_C (Fig. 6, inset B). Given the assumed high R_R (-0.5 ‰), the diluting effect

221   of riverine input on R_{SW} (R_{SW} = 0.1 ‰ at 547 Ma) is negligible at that time. However, around

222   547 Ma this trend was reversed, causing the observed increase in R_C and extremely high values

223   at the Pc-C boundary.

224   Our model shows, that the Mg ocean budget requires a very dynamic change of

225   parameters, including an incongruent increase of F_R and F_C. Taking all of these findings together,

226   a 'best-fit' of parameters was modelled (Fig. 5, inset C). This 'best-fit' model can be divided in

227   three phases (Fig. 5, inset C). In Phase I, 560 - 547 Ma, as described above, Mg removal through

228   carbonate formation (F_C) steadily decreases while weathering rates are generally elevated. This

229   causes the steady decrease in $\delta^{26}Mg_{SW}$. In Phase II, 546 – 536 Ma, this decrease was reversed by

230   steadily climbing F_C, causing an increase in $\delta^{26}Mg_{SW}$. Around 544 Ma this process was balanced

231   by increasing weathering rates, F_R, accounting for a doubling of F_R within ca. 3 Myr. Thereafter,

232   F_C and F_R rates decrease again, coupled with increasing hydrothermal removal F_H. For Phase III,

233   536 – 520 Ma, evidence of true data is missing. Thus, parameters from 536 Ma, the last observed

234   data point from this study, were kept stable converging steady state conditions. Overall, the three

235   phases mark an increase in $\delta^{26}Mg_{SW}$ with increase over ca. 15 Myr and a subsequent decrease

236   over 5 Myr with a final balance over the remaining 22 Myr, all mainly controlled by long-term

237   changes of carbonate precipitation rates and swift increases of weathering rates.

238

239   **4.2.2. $^{87}Sr/^{86}Sr$ seawater evolution**

240   Using the steady state condition for Sr in seawater (i.e., Equation 5) in Equation (3) we

241   forced the riverine (F_R) and hydrothermal (F_H) fluxes and left the diagenetic flux (F_D) constant.

242   The initial fluxes F_{in} are reported in Table 1 and represent present day values. Isotope ratios R_{in}

243   were chosen as $R_R = 0.711$ to represent increased continental weathering rates, $R_D = 0.708$ and

244    $R_H = 0.703$ according to $^{87}Sr/^{86}Sr$ seawater and mantle evolution during the Ediacaran,

245   respectively (Halverson et al., 2010; Wilson, 1989). Leaving all parameters unchanged, R_{SW}

246   rapidly increases, converging $R_{SW} = 0.7091$ and reaching near-steady state after ca. 20 Myr (Fig.

247   6, inset A). Similar to Mg, steady state conditions match the initial phase of the observed Sr

248   seawater evolution well, up to 547 Ma. Applying the same parameter changes as for the Mg

249   ocean budget, i.e., changing F_C and a swift increase in F_R, however does not satisfy the observed

250   dynamics of the Sr seawater evolution. Other than for Mg, F_R is the most powerful parameter

251   driving R_{SW} towards higher Sr isotope values, counterbalanced mainly by F_H, causing a reversed

252　trend towards lower Sr isotope values However, a steady increase in F_R does not recreate the first

253　slow increase followed by a rapid positive excursion as observed in the Sr seawater evolution

254　(Phase II). This could be achieved by a change in weathered rock-type, i.e., from a dominance of

255　less radiogenic rock types (R_R = 0.711) towards more radiogenic rock types (R_R = 0.714). This

256　could either be due to a decreased proportion of chemical weathering of carbonates, or

257　pronounced weathering of granitic material. As shown above by the Mg box model (see Section

258　4.2.1), chemical weathering of carbonates could not have been a contributing factor to riverine

259　run-off, arguing for an increased amount of basalt weathering during Phase I, which would also

260　exhibit a non-radiogenic isotope signature. Alternatively, if R_R was 0.714 from the beginning, F_H

261　would need to be significantly higher to balance the riverine input, causing the observed slower

262　increase (Fig. 6, inset A, blue line). However, we dismissed the latter possibility, as this would

263　require very sudden shifts in hydrothermal activity.

264　　　　Thus, in the 'best-fit' model the isotope ratio of the riverine input was adjusted, assuming

265　less radiogenic weathered material in the initial weathering phase followed by an increasing

266　proportion of radiogenic material as continental denudation progresses, favoring increased

267　'mineral reactivity' (cf. Caves Rugenstein et al., 2019). This 'best-fit' model also resembles the

268　three temporal phases employed for the Mg isotope systematics (Fig. 6, inset B). In Phase I, 560

269　- 547 Ma, all parameters remain in steady state at generally high weathering rates, causing the

270　R_{SW} to slowly increase. In Phase II, 546 – 536 Ma, as continental erosion progresses, more

271　radiogenic rocks are exposed. Together with rapidly increasing F_R, this causes the spike in R_{SW}.

272　The rapid increase in F_R stops at 547 Ma and returned to initial values, further balanced by the

273　continuously increasing F_H in Phase II. In Phase III, 535 – 521 Ma, similar to the Mg ocean

274　budget, F_C and F_H remain stable, with only F_R slightly increasing. In this dynamic 'best-fit', the

275   model successfully recreates the observed Sr seawater evolution, matching both magnitude and

276   short duration of the observed peak.

277

278   **5. Discussion**

279   **5.1. The significance of δ^{26}Mg composition of the riverine input**

280   Isotopically heavy δ^{26}Mg seawater values can be caused by either preferential removal of

281   light Mg isotopes, i.e. during extreme dolomitization events, or input of heavy isotopes, i.e.

282   through silicate dominated riverine influx. However, our box model needs to be confirmed by

283   both, Sr and Mg fluxes. Thus, although dolomitization may contribute to the scatter in Mg-Sr

284   isotope co-variations, it cannot be the main reason for the coupled isotope excursion, as this

285   wouldn't cause such extreme changes in the Sr isotope evolution. Despite uncertainty in the

286   input parameters, it is apparent that the isotope modelling recreates the observed amplitude at the

287   Pc-C transition.

288   Tipper et al., (2006) showed that modern rivers draining silicate rocks can be as heavy as

289   -0.3‰ in Mg isotopes and rivers draining carbonate rocks record values as low as -2.7‰. In

290   weathering dominated rivers, such as the Ganges-Brahmaputra and/or Indus that drain mixed

291   lithologies of the Himalaya, these two endmembers add to a combined riverine δ^{26}Mg of -0.9‰.

292   To evaluate the significance of the isotope ratio of riverine influx (R_C), we increase carbonate

293   removal (F_C) up to 90% of the total influx and combined this with three different possible isotope

294   ratios (R_R) of the riverine influx to represent the different endmembers from (a) carbonate

295   dominated weathering with a δ^{26}Mg value of -2.7‰, (b) silicate dominated weathering with a

296   δ^{26}Mg value of -0.3‰, and (c) a δ^{26}Mg value of -0.9‰ representing a lithologically mixed

297   weathering dominated river (Fig. 7, inset A; Tipper et al., 2008). For (a) calculated carbonate

298   δ^{26}Mg values are unrealistically low with an average of -4.9 ± 0.7 ‰ (2SD, n=39) and display

299   the opposite trend of the observed Mg evolution. Thus, we argue that weathering of carbonates

300   could not have played a significant role during the Pc-C time period. In turn, as suggested in the

301   'best-fit' model for Sr seawater evolution, a shift from the weathering of basalt dominated

302   catchment towards a granite dominated one would not affect the δ^{26}Mg composition of riverine

303   run-off. Using the δ^{26}Mg value of the silicate weathering dominated Scenarios (b) and (c), it was

304   possible to recreate a more sensible trend (Fig. 7). The 'best-fit' was calculated with an R_R value

305   of -0.5‰ for δ^{26}Mg, representing an intermediate value between a purely silicate dominated

306   weathering (Scenario b) regime and a lithologically mixed weathering dominated regime

307   (Scenario c), which would validate the observed Sr-Mg isotope systematics.

308

309   **5.2. Mg isotopes as a palaeo-environmental proxy in ancient sediments**

310   Although Mg isotopes have become a rather routine geochemical tool, its

311   application/suitability as an environmental proxy for ancient sedimentary archives is still being

312   explored (Kasemann et al., 2014; Pokrovsky et al., 2011). Reconstruction of the δ^{26}Mg values of

313   past seawater from carbonate deposits is highly challenging, as Mg isotope fractionation between

314   the precipitated carbonate and ambient solution depends on multiple factors, e.g., temperature,

315   precipitation rate and/or alkalinity, as well as burial depth (Blättler et al., 2015; Mavromatis et

316   al., 2013). For these reasons, comparison of absolute values should be regarded with caution.

317   However, trends and relative variations can be reasonably assessed. Pokrovsky et al., (2011)

318   hypothesized that Mg isotope composition of Late Neoproterozoic sedimentary rocks or

319   limestones/dolostones was mainly controlled by the weathering conditions and regime, i.e.

320   carbonate vs. silicate weathering. The herein modeled δ^{26}Mg$_{carb}$ values show a similar trend as

321   the observed values at the Pc-C boundary (Figs. 5 and 6). For the Mg box model, the isotope

322   composition of riverine input is crucial to the seawater δ^{26}Mg mass balance, revealing the

323   important effect of continental silicate weathering on the observed δ^{26}Mg trend. Moreover, it

324   excludes weathered carbonates (limestones and dolostones) as a major contributing factor to

325   riverine run-off.

326   Our isotope modelling suggests that the ocean budget for Mg was close to steady state

327   before and after the Pc-C boundary. During the transition, the Mg ocean budget was controlled

328   by a simultaneous but incongruent increase of F_R and F_C, and consequently increasing

329   hydrothermal activity (Fig. 5). As shown above (Section 4.2), this environmental scenario

330   satisfies both Sr and Mg isotope trends in seawater, providing a feasible and coherent scenario

331   for the observed isotope excursion. The conformity of both isotope systems (Mg and Sr) further

332   justifies the use of Mg isotopes as a valid environmental proxy. However, due to the lack of

333   comparison to other locations, the observed Mg isotope trend may have been driven by regional

334   factors and may not be applicable to a global scale. Nonetheless, our study highlights the

335   potential of Mg isotope investigations at the Pc-C boundary, and at similar critical episodes in

336   Earth's environmental history. As for most environmental proxies and especially for their

337   applicability in ancient rocks, Mg isotopes should be applied within multi-proxy approaches.

338

339   **5.3. The impact of silicate weathering on isotopic records**

340   A global increase in continental weathering, as highlighted by a range of studies (Shields,

341   2007; Williams et al., 2019; Zhang et al., 2014), over the Pc-C transition affected individual δ^{13}C

342   records within the litho- and hydrosphere. In general, secular (long-term) changes in the δ^{13}C

343   records of carbonate deposits reflect mostly mixing of the organic and inorganic carbon pool,

344 closely linked to climate changes, i.e., glacial and interglacial times. However, tectonic uplift and

345 burial can also significantly affect the global carbon flux and mass balance (Shields and Mills,

346 2017). Simply speaking, increased continental reworking and thus a (silicate-) dominated

347 riverine run-off into the ocean, as well as an increased supply of major nutrients enhance primary

348 productivity in surface waters, effectively removing ^{12}C from the ocean causing high $\delta^{13}C$. Yet,

349 the Pc-C boundary is marked by the negative basal Cambrian carbon excursion (BACE), also

350 observed at the Koksu location (Fig. 2; Stammeier et al., 2019a). Generally, such a negative

351 excursion towards more lighter $\delta^{13}C$ values in seawater is attributed to the oxidation of organic

352 carbon, and/or the reworking of shallow-water carbonates during a transgression cycle (Hoefs,

353 2015; Pokrovsky et al., 2011; Zuo et al., 2018). Shields and Mills (2017) have shown that carbon

354 contribution from intense silicate weathering outweighs the positive feedback loop of organic

355 carbon removal. Given the significant contribution of silicate weathering to the ocean's Mg and

356 Sr budgets, as suggested in our model, this could be a likely scenario for the Pc-C boundary.

357 Such an increase of continental silicate weathering caused the simultaneous increase of $\delta^{26}Mg$

358 and $^{87}Sr/^{86}Sr$ and decrease of $\delta^{13}C$ as observed at the Pc-C boundary (Fig. 2).

359

360 **6. Palaeoenvironmental implications: long-term versus short-term environmental changes**

361   Enhanced erosion rates are expected in the aftermath of several Neoproterozoic

362 glaciations, such as e.g., during the Sturtian and Marinoan (Kasemann et al., 2014), and as a

363 consequence of Gondwana assembly from 0.8-0.6 Ga (Meert and Van Der Voo, 1997).

364 Weathering and associated riverine run-off were thus the likely cause for the steady increase in

365 Sr isotopes during the late Neoproterozoic era (cf. Halverson et al., 2010) along with an increase

366   in ocean alkalinity and transport of nutrients, e.g., phosphorus, to the oceans (Smith and Harper,

367   2013).

368   The sharp excursion in seawater $^{87}Sr/^{86}Sr$ together with high $\delta^{26}Mg$ at the Pc-C transition

369   (Fig. 2), however, indicates a single, critical geodynamic event. As demonstrated in our model, a

370   short yet extreme change in all parameters (F_C, F_R, R_R), can result in the observed isotope trends.

371   In the case of the Sr ocean budget, a time-interval of only 3 Myr of increased (silicate)

372   weathering and associated "mineral reactivity" during this process was sufficient to trigger Sr

373   isotope excursions. This cannot be solely explained by secular trends in enhanced weathering

374   rates during the Neoproterozoic, but required a distinct geodynamic event. The timing coincided

375   with a range of global orogenies, e.g., the Pan-African orogeny (ca. 870-550 Ma, Kröner and

376   Stern, 2005), and the Cadomian orogeny (750-540 Ma, Linnemann et al., 2014), associated with

377   the assembly of Gondwana. Whilst current geotectonic plate reconstruction lacks the temporal

378   resolution to pinpoint a single, unique collisional event, the negative excursion in e.g., the global

379   Hf isotope data, indicates an unprecedented collision of continental landmass at the time of

380   Gondwana assembly (Roberts, 2012). Such a collisional event and the associated crustal

381   reworking, including uplift, exposure, weathering and erosion, would have caused an increase of

382   riverine input to the ocean, resulting in high, short-term $^{87}Sr/^{86}Sr$ and $\delta^{26}Mg$ values in the ocean.

383

7. Conclusions

385   Shallow-marine sedimentary deposits from the lowermost Cambrian succession close to

386   the Pc-C boundary recorded coupled $^{87}Sr/^{86}Sr$ and $\delta^{26}Mg$ values with a distinct, positive isotope

387   excursion. Isotope modelling demonstrated that the Pc-C transition was dominated by elevated

388   weathering rates and carbonate formation. The positive excursions in seawater $^{87}Sr/^{86}Sr$ and

389   δ^{26}Mg were caused by a short-term (ca. 3 Myr) increase in weathering rates and associated

390   transport of weathered riverine material to the ocean. This resulted in distinctly high seawater

391   ^{87}Sr/^{86}Sr and δ^{26}Mg, which was rapidly counterbalanced by enhanced hydrothermal activity.

392   Modelling of seawater ^{87}Sr/^{86}Sr further suggests a shift from less radiogenic towards more

393   radiogenic weathered material in the lead-up to the Pc-C transition. Together with elevated

394   weathering rates, this agrees with progressing continental reworking and denudation in the

395   aftermath of several global-scale glaciations and continental re-organization.

396   The modelled isotope data from the current study does only offer a first order, qualitative

397   approximation, and in the case of Mg isotopes, might only reflect a local mechanism. However,

398   the ^{87}Sr/^{86}Sr seawater evolution together with the model results for both Mg and Sr do support a

399   severe, global-scale geodynamic event. The observed isotope excursions marking the Pc-C

400   boundary at 541 Ma appear unique, both in their magnitude and relatively short duration. With

401   this, they mirror the rapid biotic changes that occurred during the terminal Ediacaran and earliest

402   Cambrian. It thus seems plausible that a geodynamic event, in this case continental collision

403   along with reworking of evolved continental crust and an associated release of nutrients, led to a

404   turnover in marine biota during the Pc-C transition.

405

415

416 **References**

417   Aciego, S.M., Bourdon, B., Lupker, M., Rickli, J., 2009. A new procedure for separating and

418   measuring radiogenic isotopes (U, Th, Pa, Ra, Sr, Nd, Hf) in ice cores. Chem. Geol. 266,

419   203–213. https://doi.org/10.1016/j.chemgeo.2009.06.003

420   Berner, R.A., Lasaga, A.C., Garrels, R.M., 1983. The carbonate-silicate geochemical cycle and

421   its effect on atmospheric carbon dioxide over the past 100 million years. Am. J. Sci. 283,

422   641–683. https://doi.org/10.2475/ajs.283.7.641

423   Blättler, C.L., Miller, N.R., Higgins, J.A., 2015. Mg and Ca isotope signatures of authigenic

424   dolomite in siliceous deep-sea sediments. Earth Planet. Sci. Lett. 419, 32–42.

425   https://doi.org/10.1016/J.EPSL.2015.03.006

426   Brasier, M.D., Shields, G.A., Kuleshov, V.N., Zhegallo, E.A., 1996. Integrated chemo- and

427   biostratigraphic calibration of early animal evolution: Neoproterozoic–early Cambrian of

428   southwest Mongolia. Geol. Mag. 133, 445–485.

429   https://doi.org/10.1017/S0016756800007603

430   Burns, S.J., Haudenschild, U., Matter, A., 1994. The strontium isotopic composition of

431   carbonates from the late Precambrian (560-540Ma) Huqf Group of Oman. Chem. Geol. 111,

432   269–282. https://doi.org/10.1016/0009-2541(94)90094-9

433   Caves Rugenstein, J.K., Ibarra, D.E., von Blanckenburg, F., 2019. Neogene cooling driven by

434   land surface reactivity rather than increased weathering fluxes. Nature 571, 99–102.

435   https://doi.org/10.1038/s41586-019-1332-y

436   Darroch, S.A.F., Smith, E.F., Laflamme, M., Erwin, D.H., 2018. Ediacaran Extinction and

437   Cambrian Explosion. Trends Ecol. Evol. 33, 653–663.

438   https://doi.org/10.1016/J.TREE.2018.06.003

439   de Villiers, S., Dickson, J.A.D., Ellam, R.M., 2005. The composition of the continental river

440   weathering flux deduced from seawater Mg isotopes. Chem. Geol. 216, 133–142.

441   https://doi.org/10.1016/j.chemgeo.2004.11.010

442   Derry, L.A., Brasier, M.D., Corfield, R.M., Rozanov, A.Y., Zhuravlev, A.Y.Y., 1994. Sr and C

443   isotopes in Lower Cambrian carbonates from the Siberian craton: A paleoenvironmental

444   record during the "Cambrian explosion." Earth Planet. Sci. Lett. 128, 671–681.

445   https://doi.org/10.1016/0012-821X(94)90178-3

446   Eganov, E.A., Sovetov, K.Y., Yanshin, A.L., 1986. Proterozoic and Cambrian phosphorite

447   deposits: Karatau, southern Kazakhstan, USSR, in: Cook, P.J., Shergold, J.H. (Eds.),

448   Phosphate Deposits of the World. Cambridge University Press, Cambridge, pp. 175–189.

449   Fantle, M.S., Higgins, J.A., 2014. The effects of diagenesis and dolomitization on Ca and Mg

450   isotopes in marine platform carbonates: Implications for the geochemical cycles of Ca and

451   Mg. Geochim. Cosmochim. Acta 142, 458–481. https://doi.org/10.1016/j.gca.2014.07.025

452   Farkaš, J., Chakrabarti, R., Jacobsen, S.B., Kump, L.R., Melezhik, V.A., 2013. Ca and Mg

453   Isotopes in Sedimentary Carbonates, in: Melezhik, V.A. (Ed.), Reading the Archive of

454   Earth's Oxygenation. Springer-Verlag Berlin, Heidelberg, pp. 1468–1482.

455   https://doi.org/10.1007/978-3-642-29670-3_10

456   Fox, D., 2016. What sparked the Cambrian explosion? Nature 530, 268–270.

457   https://doi.org/10.1038/530268a

458   Geske, A., Goldstein, R.H., Mavromatis, V., Richter, D.K., Buhl, D., Kluge, T., John, C.M.,

459   Immenhauser, A., 2015a. The magnesium isotope (δ26Mg) signature of dolomites.

460   Geochim. Cosmochim. Acta 149, 131–151. https://doi.org/10.1016/j.gca.2014.11.003

461   Geske, A., Lokier, S., Dietzel, M., Richter, D.K., Buhl, D., Immenhauser, A., 2015b. Magnesium

462   isotope composition of sabkha porewater and related (Sub-)Recent stoichiometric

463   dolomites, Abu Dhabi (UAE). Chem. Geol. 393–394, 112–124.

464   https://doi.org/10.1016/j.chemgeo.2014.11.020

465   Halverson, G.P., Hurtgen, M.T., Porter, S.M., Collins, A.S., 2009. Neoproterozoic-Cambrian

466   Biogeochemical Evolution, in: Gaucher, C., Sial, A.N., Frimme, H.E., Halverson, G.P.

467   (Eds.), Neoproterozoic-Cambrian Tectonics, Global Change And Evolution: A Focus On

468   South Western Gondwana. Developments in Precambrian Geology, pp. 351–365.

469   https://doi.org/10.1016/S0166-2635(09)01625-9

470   Halverson, G.P., Wade, B.P., Hurtgen, M.T., Barovich, K.M., 2010. Neoproterozoic

471   chemostratigraphy. Precambrian Res. 182, 337–350.

472   https://doi.org/10.1016/j.precamres.2010.04.007

473   Heubeck, C., Ergaliev, G., Evseev, S., 2013. Large-Scale Seismogenic Deformation of A

474   Carbonate Platform Straddling the Precambrian-Cambrian Boundary, Karatau Range,

475   Kazakhstan. J. Sediment. Res. 83, 1004–1024. https://doi.org/10.2110/jsr.2013.76

476   Higgins, J.A., Schrag, D.P., 2010. Constraining magnesium cycling in marine sediments using

477   magnesium isotopes. Geochim. Cosmochim. Acta 74, 5039–5053.

478   https://doi.org/10.1016/j.gca.2010.05.019

479   Hodell, D.A., Mueller, P.A., McKenzie, J.A., Mead, G.A., 1989. Strontium isotope stratigraphy

480   and geochemistry of the late Neogene ocean. Earth Planet. Sci. Lett. 92, 165–178.

481   https://doi.org/10.1016/0012-821X(89)90044-7

482   Hoefs, J., 2015. Stable Isotope Geochemistry. Springer International Publishing, Cham.

483   https://doi.org/10.1007/978-3-319-19716-6

484   Jackson, P., Attalla, M.I., 2010. N-Nitrosopiperazines form at high pH in post-combustion

485   capture solutions containing piperazine: a low-energy collisional behaviour study. Rapid

486   Commun. Mass Spectrom. 24, 3567–3577. https://doi.org/10.1002/rcm

487   Kasemann, S.A., Pogge von Strandmann, P.A.E., Prave, A.R., Fallick, A.E., Elliott, T.,

488   Hoffmann, K.H., 2014. Continental weathering following a Cryogenian glaciation:

489   Evidence from calcium and magnesium isotopes. Earth Planet. Sci. Lett. 396, 66–77.

490   https://doi.org/10.1016/j.epsl.2014.03.048

491   Kröner, A., Stern, R.J., 2005. AFRICA | Pan-African Orogeny, in: Encyclopedia of Geology.

492   Elsevier, pp. 1–12. https://doi.org/10.1016/B0-12-369396-9/00431-7

493   Laflamme, M., Darroch, S.A.F., Tweedt, S.M., Peterson, K.J., Erwin, D.H., 2013. The end of the

494   Ediacara biota: Extinction, biotic replacement, or Cheshire Cat? Gondwana Res. 23, 558–

495   573. https://doi.org/10.1016/j.gr.2012.11.004

496   Li, D., Ling, H.-F., Shields-Zhou, G.A., Chen, X., Cremonese, L., Och, L., Thirlwall, M.,

497   Manning, C.J., 2013. Carbon and strontium isotope evolution of seawater across the

498   Ediacaran–Cambrian transition: Evidence from the Xiaotan section, NE Yunnan, South

499   China. Precambrian Res. 225, 128–147. https://doi.org/10.1016/j.precamres.2012.01.002

500   Li, W., Beard, B.L., Li, C., Xu, H., Johnson, C.M., 2015. Experimental calibration of Mg isotope

501   fractionation between dolomite and aqueous solution and its geological implications.

502   Geochim. Cosmochim. Acta 157, 164–181. https://doi.org/10.1016/J.GCA.2015.02.024

503   Linnemann, U., Gerdes, A., Hofmann, M.H., Marko, L., 2014. The Cadomian Orogen:

504   Neoproterozoic to Early Cambrian crustal growth and orogenic zoning along the periphery

505   of the West African Craton—Constraints from U–Pb zircon ages and Hf isotopes

506   (Schwarzburg Antiform, Germany). Precambrian Res. 244, 236–278.

507   https://doi.org/10.1016/j.precamres.2013.08.007

508 Mavromatis, V., Gautier, Q., Bosc, O., Schott, J., 2013. Kinetics of Mg partition and Mg stable

509   isotope fractionation during its incorporation in calcite. Geochim. Cosmochim. Acta 114,

510   188–203. https://doi.org/10.1016/j.gca.2013.03.024

511 Mavromatis, V., Meister, P., Oelkers, E.H., 2014. Using stable Mg isotopes to distinguish

512   dolomite formation mechanisms: A case study from the Peru Margin. Chem. Geol. 385, 84–

513   91. https://doi.org/10.1016/j.chemgeo.2014.07.019

514 Meert, J.G., Van Der Voo, R., 1997. The assembly of Gondwana 800-550 Ma. J. Geodyn. 23,

515   223–235. https://doi.org/10.1016/S0264-3707(96)00046-4

516 Nicholas, C.J., 1996. The Sr isotopic evolution of the oceans during the "Cambrian Explosion."

517   J. Geol. Soc. London. 153, 243–254. https://doi.org/10.1144/gsjgs.153.2.0243

518 Palmer, M.R., Edmond, J.M., 1989. The strontium isotope budget of the modern ocean. Earth

519   Planet. Sci. Lett. 92, 11–26. https://doi.org/10.1016/0012-821X(89)90017-4

520 Pogge von Strandmann, P.A.E., 2008. Precise magnesium isotope measurements in core top

521   planktic and benthic foraminifera. Geochemistry, Geophys. Geosystems 9, 1–13.

522   https://doi.org/10.1029/2008GC002209

523 Pogge von Strandmann, P.A.E., Forshaw, J., Schmidt, D.N., 2014. Modern and Cenozoic records

524   of seawater magnesium from foraminiferal Mg isotopes. Biogeosciences 11, 5155–5168.

525   https://doi.org/10.5194/bg-11-5155-2014

526 Pokrovsky, B.G., Mavromatis, V., Pokrovsky, O.S., 2011. Co-variation of Mg and C isotopes in

527   late Precambrian carbonates of the Siberian Platform: A new tool for tracing the change in

528   weathering regime? Chem. Geol. 290, 67–74.

529   https://doi.org/10.1016/j.chemgeo.2011.08.015

530   Richter, F.M., Rowley, D.B., DePaolo, D.J., 1992. Sr isotope evolution of seawater: the role of

531   tectonics. Earth Planet. Sci. Lett. 109, 11–23. https://doi.org/10.1016/0012-821X(92)90070-

532   C

533   Roberts, N.M.W., 2012. Increased loss of continental crust during supercontinent amalgamation.

534   Gondwana Res. 21, 994–1000. https://doi.org/10.1016/j.gr.2011.08.001

535   Sawaki, Y., Ohno, T., Fukushi, Y., Komiya, T., Ishikawa, T., Hirata, T., Maruyama, S., 2008. Sr

536   isotope excursion across the Precambrian-Cambrian boundary in the Three Gorges area,

537   South China. Gondwana Res. 14, 134–147. https://doi.org/10.1016/j.gr.2007.11.002

538   Shields, G.A., 2007. A normalised seawater strontium isotope curve: possible implications for

539   Neoproterozoic-Cambrian weathering rates and the further oxygenation of the Earth. eEarth

540   2, 35–42. https://doi.org/10.5194/ee-2-35-2007

541   Shields, G.A., Mills, B.J.W., 2017. Tectonic controls on the long-term carbon isotope mass

542   balance. Proc. Natl. Acad. Sci. 114, 4318–4323. https://doi.org/10.1073/pnas.1614506114

543   Smith, M.P., Harper, D.T., 2013. Causes of the Cambrian Explosion. Science (80-.). 341, 1355–

544   1356. https://doi.org/10.1126/science.1239450

545   Stammeier, J.A., Hippler, D., Nebel, O., Leis, A., Grengg, C., Mittermayr, F., Kasemann, S.A.,

546   Dietzel, M., 2019a. Radiogenic Sr and Stable C and O Isotopes Across Precambrian-

547   Cambrian Transition in Marine Carbonatic Phosphorites of Malyi Karatau (Kazakhstan)-

548   Implications for Paleo-environmental Change. Geochemistry, Geophys. Geosystems 20, 3–

549   23. https://doi.org/10.1029/2018GC007767

550   Stammeier, J.A., Nebel, O., Hippler, D., Dietzel, M., 2019b. Stable magnesium and radiogenic

551   strontium isotopes in carbonate bearing geologic reference materials (SARM 40, SARM 43,

552   SRM 88A, SRM 88B) (submitted). MethodsX.

553   Tipper, E.T., Galy, A., Bickle, M.J., 2008. Calcium and magnesium isotope systematics in rivers

554   draining the Himalaya-Tibetan-Plateau region: Lithological or fractionation control?

555   Geochim. Cosmochim. Acta 72, 1057–1075. https://doi.org/10.1016/j.gca.2007.11.029

556   Tipper, E.T., Galy, A., Bickle, M.J., 2006a. Riverine evidence for a fractionated reservoir of Ca

557   and Mg on the continents: Implications for the oceanic Ca cycle. Earth Planet. Sci. Lett.

558   247, 267–279. https://doi.org/10.1016/j.epsl.2006.04.033

559   Tipper, E.T., Galy, A., Gaillardet, J., Bickle, M.J., Elderfield, H., Carder, E.A., 2006b. The

560   magnesium isotope budget of the modern ocean: Constraints from riverine magnesium

561   isotope   ratios.   Earth   Planet.   Sci.   Lett.   250,   241–253.

562   https://doi.org/10.1016/j.epsl.2006.07.037

563   Wilkinson, B.H., Algeo, T.J., 1989. Sedimentary carbonate record of calcium-magnesium

564   cycling. Am. J. Sci. 289, 1158–1194. https://doi.org/10.2475/ajs.289.10.1158

565   Williams, J.J., Mills, B.J.W., Lenton, T.M., 2019. A tectonically driven Ediacaran oxygenation

566   event. Nat. Commun. 10, 2690. https://doi.org/10.1038/s41467-019-10286-x

567   Wilson, M.B., 1989. Igneous Petrogenesis. Springer Netherlands, Dordrecht.

568   https://doi.org/10.1007/978-1-4020-6788-4

569   Wimpenny, J., Yin, Q.Z., Tollstrup, D., Xie, L.W., Sun, J., 2014. Using Mg isotope ratios to

570   trace Cenozoic weathering changes: A case study from the Chinese Loess Plateau. Chem.

571   Geol. 376, 31–43. https://doi.org/10.1016/j.chemgeo.2014.03.008

572   Wombacher, F., Eisenhauer, A., Heuser, A., Weyer, S., 2009. Separation of Mg, Ca and Fe from

573   geological reference materials for stable isotope ratio analyses by MC-ICP-MS and double-

574   spike TIMS. J. Anal. At. Spectrom. 24, 627–636. https://doi.org/10.1039/b820154d

575 Zhang, X., Shu, D., Han, J., Zhang, Z., Liu, J., Fu, D., 2014. Triggers for the Cambrian

576   explosion: Hypotheses   and   problems.   Gondwana   Res.   25,   896–909.

577   https://doi.org/10.1016/j.gr.2013.06.001

578 Zuo, J., Peng, S., Qi, Y., Zhu, X., Bagnoli, G., Fang, H., 2018. Carbon-Isotope Excursions

579   Recorded in the Cambrian System, South China: Implications for Mass Extinctions and

580   Sea-Level Fluctuations. J. Earth Sci. 29, 479–491. https://doi.org/10.1007/s12583-017-

581   0963-x

582

583   **Figure captions**

584   **Figure 1** Schematic geologic map of the Malyi and Bolshoi Karatau Mountain range

585 (simplified after Eganov and Sovetov, 1986). The Koksu section (43.653611, 69.636389,

586 WGS84) is located at the margin of a former shallow-water basin.

587

588   **Figure 2** Compiled isotope profile of the investigated Koksu section. Both Mg-Sr and C-

589 O isotopes display the same temporal trend, calculated as the moving average (black line). The

590 orange shading indicates the timing of the basal Cambrian carbon event (BACE). Sr, C and O

591 isotope data from Stammeier et al. (2019a). Ky. Fm = Kyrshabakty formation, AC = Aksai

592 Chert, LP = Lower Phosphorite, SM = Shale Member after (Heubeck et al., 2013). If not

593 indicated otherwise, uncertainty (2 SD) is within symbol size.

594

595   **Figure 3** Mg and Sr isotope composition of two samples treated with weak acid (0.05

596 mol l^{-1} HNO_3; squares) and stronger acid (3 mol l^{-1} HNO_3; circles). Error bars for $\delta^{26}Mg$ are

597   ±0.10 ‰ and refer to the reproducibility of reference material Cambridge-1 (Romil Ltd.,

598   Cambridge, UK). Sr isotope values and respective uncertainties from (Stammeier et al., 2019a).

599

600

601   **Figure 4** Cross plots of $\delta^{26}Mg$ vs. $^{87}Sr/^{86}Sr$ and $\delta^{18}O$. Note that the bulk of data does not

602   show any correlation.

603

604   **Figure 5** Calculated Mg isotope values in a time-dependent dynamic state model. Red

605   circles indicate isotope ratios measured in early Cambrian Kazakh strata (this study). Bright blue

606   line: $\delta^{26}Mg$ values of dolomites from the Siberian platform taken from Pokrovsky et al., (2011).

607   Note that the age of these values could only be estimated linearly. Blue line (R_{SW}) represents

608   modelled $\delta^{26}Mg$ seawater evolution, with the respective carbonates (R_C, green line), in response

609   to dynamic carbonate removal (F_C) and hydrothermal activity (F_H), shown as F_C/F_H (grey line).

610   Note the different scales of the primary and secondary abscissae in the insets. Inset A: modelled

611    $\delta^{26}Mg$ at steady state conditions. Inset B: Modelled $\delta^{26}Mg$ show significant variation when

612   carbonate removal F_C is increased. The reversed trend of R_{SW} at 536 Ma is produced when $F_C >$

613   F_R. Inset C: 'best-fit' of modelled $\delta^{26}Mg$. Note that R_R remains constant up to 545 Ma.

614

615   **Figure 6** Calculated Sr isotope values in a time-dependent dynamic state model. Red

616   circles indicate isotope ratios measured in early Cambrian Kazakh strata. Thick blue line

617   indicates recorded $^{87}Sr/^{86}Sr$ seawater evolution as compiled by Stammeier et al. (2019a) and

618   references therein. Inset A: modelled $^{87}Sr/^{86}Sr$ seawater at steady state conditions, calculated

619   using R_R = 0.714 (blue line) and R_R = 0.711 (black line). Inset B: modelled $^{87}Sr/^{86}Sr$ seawater

620   evolution matches the observed $^{87}Sr/^{86}Sr$ seawater evolution.

621

622   **Figure 7** Modelled $\delta^{26}Mg$ in carbonates (R_C) using different parameters. Inset A:

623   evolution of R_C when applying different riverine (R_R) input values, representing carbonate,

624   silicate, generally or mixed weathering dominated endmembers, in comparison to 'best-fit'

625   results (thick green line). Inset B: considering a larger fractionation factor, e.g., representing

626   calcite precipitation, the amplitude of the modelled $\delta^{26}Mg$ becomes significantly larger. Note that

627   for this latter calculation same parameters as for the 'best-fit' were used.

628

629   **Table captions**

630

631   **Table 1** Parameter values used in the time-dependent dynamic state model. .

632

APPENDIX A:

ELEMENTAL AND ISOTOPE INFORMATION

Element and isotope compositions were determined on 3 mol l^{-1} HNO_3 leachates (compare methodology section). Main elemental concentrations reflect dissolution of mainly calcite, dolomite and carbonate-fluorapatite (CFA) and only trace amounts of detrital silicate cargo, that could contribute to bulk Mg isotope composition (compare table A2). Total main elemental concentrations were analysed at the Graz University of Technology by ICP-OES using an Optima 8300 (PerkinElmer, Waltham, USA) with an analytical precision of ± 2%.

Table A1 Total main elemental concentrations of the acid soluble fraction (3 mol l^{-1} HNO_3; all elemental data from Stammeier at al. 2018. The abundance of CO_2 within the carbonates and phosphates was estimated from difference. n.a. = not available; DL = detection limit.

Sample	Al_2O_3 (wt. %)	CaO (wt. %)	Fe_2O_3 (wt. %)	MgO (wt. %)	Na_2O (wt. %)	P_2O_5 (wt. %)	SiO_2 (wt. %)	SUM (wt. %)	CO_2 (wt. %)
KO 1	0.36	49.6	5.09	4.57	0.59	37.8	0.21	98.2	1.80
KO 2	0.34	46.9	0.26	0.89	0.37	40.4	0.11	89.3	10.7
KO 3.1	0.42	41.1	0.16	6.44	D.L.	37.9	0.30	86.4	0.42
KO 3.2	0.30	46.1	1.46	2.37	0.28	37.0	0.03	87.5	12.5
KO 04	0.07	30.0	0.21	19.1	0.06	1.50	0.07	51.0	49.0
KO 6	0.28	48.5	2.48	2.87	0.23	35.2	0.04	89.6	10.4
KO 9	0.07	37.7	0.09	2.68	0.20	29.2	0.08	90.2	9.80
KO 10.1*	n.a.	n.a.	n.a.	n.a.	n.a.	n.a.	n.a.	n.a.	n.a.
KO 10.2*	0.06	73.0	0.02	2.34	0.21	28.5	0.08	70.0	30.0
KO 11	0.04	43.0	0.01	2.98	0.21	35.9	0.03	104	n.a.
KO 12	0.03	39.1	0.01	5.99	0.18	27.7	0.03	82.2	17.8
KO 13.1*	n.a.	n.a.	n.a.	n.a.	n.a.	n.a.	n.a.	n.a.	n.a.
KO 13.2*	0.04	42.6	0.02	5.25	0.27	29.7	0.09	73.0	27.0.

n.a.= not analysed; * sample KO10.1 and KO13.1 reflect results from weak acid leachates (0.05 mol l^{-1} HNO_3), KO10.2 and KO13.2 reflect results from strong acid leachates (3 mol l^{-1} HNO_3, compare methodology section)

Table A2 Lithologic description of hand specimens and respective qualitative XRD results determining major mineral phases. Note that the order of minerals does not reflect quantitative results. Magnesium contents of the acid-soluble fraction (3 mol l^{-1} HNO_3) are as reported in Stammeier et al. (2018). Mg isotopes ($\delta^{25}Mg$ and $\delta^{26}Mg$ in ‰ DSM3) are reported as the mean of replica measurements with the uncertainty, expressed as 2 SD, referring to the standard deviation of the mean. In case the uncertainty of replica measurements is lower than the repeatability precision, values marked with *, the repeatability precision of ±0.04‰ for $\delta^{25}Mg$ and ±0.10‰ for $\delta^{26}Mg$ (2 SD, n=23) for CAM-1 is reported.

Sample	Lithologic description	Mineralogy	MgO [wt. %]	$\delta^{25}Mg$ (‰DSM3)	±2SD	$\delta^{26}Mg$ (‰DSM3)	±2SD
KO 1	phosphatic chert	quartz, CFA, calcite	4.57	-0.21*	0.04	-0.45*	0.10
KO 2	phosphatic chert	quartz, CFA, calcite	0.89	-0.04*	0.04	0.06	0.12
KO 3.1	phosphatic chert	quartz, CFA, dolomite, calcite	2.37	-0.37	0.05	-0.77*	0.10
KO 3.2	phosphatic chert	n.a.	n.a	0.25	0.04	0.48*	0.10
KO 04	cherty dolostone	quartz, CFA, dolomite	19.1	-0.34	0.09	-0.66	0.17
KO 6	phosphatic chert	quartz, CFA,	2.87	-0.23	0.22	-0.49	0.28

KO 9	phosphatic platy chert	dolomite, calcite quartz, CFA, dolomite, calcite	2.68	-1.16*	0.04	-2.12*	0.10
KO 10.1*	contact dolostone/ phosphorite	quartz, CFA, dolomite, calcite	2.34	-0.59	0.05	-1.15*	0.10
KO 10.2*	phosphorite	n.a.	n.a	-0.65*	0.04	-1.24*	0.10
KO 11	phosphorite	quartz, CFA, dolomite, calcite,	2.98	-1.01*	0.04	-1.91*	0.10
KO 12	dolomitic phosphorite	quartz, CFA, dolomite, calcite,	5.99	-0.66*	0.04	-1.42*	0.10
KO 13.1*	phosphatic flat pebble conglomerate	quartz, CFA, dolomite, calcite	5.25	-0.90*	0.04	-1.85*	0.10
KO 13.2*	phosphatic flat pebble conglomerate	n.a.	n.a	-0.90	0.06	-1.69*	0.10

n.a.= not analysed; * sample KO10.1 and KO13.1 reflect results from weak acid leachates (0.05 mol l^{-1} HNO$_3$), KO10.2 and KO13.2 reflect results from strong acid leachates (3 mol l^{-1} HNO$_3$, compare methodology section)

PETROGRAPHY

The investigated phosphatic rock samples predominantly consist of different phos-grains of various grain size, with a calcite, dolomite or siliceous matrix. Phos-grains are often preserved as clasts (Fig. A1, Inset A and B), peloids or coated grains, such as oncoids and ooids. Scanning electron microscopy (SEM) images of phos-ooids and phos-peloids reveal the preservation of CFA nano-crystals, either as radially arranged prismatic CFA nanocrystals within the laminae of ooids (Fig. A1, Inset C) or as aggregated CFA nanocrystals within phos-peloids (Fig. A1, Inset D). Silica or dolomite cements the intergranular space. Rock fabrics thus consist of siliceous mudstone to grainstone phosphorite, the latter ranging from well-sorted phos-grainstones (Fig. A1, Inset B) to poorly sorted flat-pebble phos-rudstones (Fig. A1, Inset A). These rock fabrics indicate deposition in a shallow water environment, with pronounced phosphogenesis and subsequent reworking and deposition within a moderately to high energy setting.
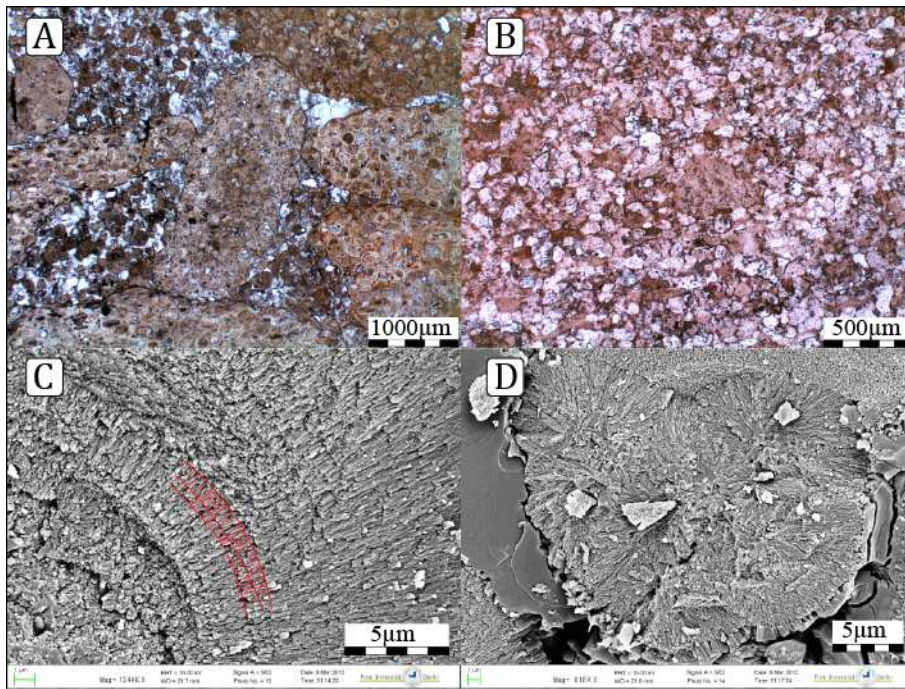
Figure A1 Inset A: Poorly sorted flat-pebble phos-rudstone (KO 13) with a sparry dolomite matrix. Inset B: Well sorted phos- grainstone, with phos-clasts and few coated phos-grains within a sparry calcite cement (KO10, stained with Alizarin Red S). Inset C: Detailed SEM image of a phos-ooid showing the well preserved prismatic CFA nanocrystals radially arranged within the laminae (KO13). Inset D: SEM image of a phos-peloid highlighting the radially-aggregated CFA nanocrystals (KO13).

	Parameter	Sr [1]	Mg [4]
Source*:	F_R (mol yr⁻¹)	$3.3*10^{10}$	$5.6*10^{12}$
	F_D (mol yr⁻¹)	$0.3*10^{10}$	$2.8*10^{12}$
	F_H (mol yr⁻¹)	$1.0*10^{10}$	$2.8*10^{12}$
	N (mol)	$1.25*10^{17}$	$7.3*10^{19}$
		$^{87}Sr/^{86}Sr$ [2,3]	$\delta^{26}Mg$ [5,6,7]
Isotope ratios*:	R_R	0.711	-0.5‰
	R_C	0.708	-2.0‰
	R_H	0.703	
	R_N		0.8‰

*Subscript refers to the respective reservoir with R = riverine, D = diagenetic, H = hydrothermal;
[1] Richter et al., 1992; [2] Halverson et al., 2010; [3] Wilson, 1989; [4] Wilkinson and Algeo, 1989; [5] Wimpenny et al., 2014; [6] Tipper et al., 2006; [7] Pokrovsky et al., 2011

Halverson, G.P., Wade, B.P., Hurtgen, M.T., Barovich, K.M., 2010. Neoproterozoic chemostratigraphy. Precambrian Res. 182, 337–350. https://doi.org/10.1016/j.precamres.2010.04.007

Pokrovsky, B.G., Mavromatis, V., Pokrovsky, O.S., 2011. Co-variation of Mg and C isotopes in late Precambrian carbonates of the Siberian Platform: A new tool for tracing the change in weathering regime? Chem. Geol. 290, 67–74. https://doi.org/10.1016/j.chemgeo.2011.08.015

Richter, F.M., Rowley, D.B., DePaolo, D.J., 1992. Sr isotope evolution of seawater: the role of tectonics. Earth Planet. Sci. Lett. 109, 11–23. https://doi.org/10.1016/0012-821X(92)90070-C

Tipper, E.T., Galy, A., Gaillardet, J., Bickle, M.J., Elderfield, H., Carder, E.A., 2006. The magnesium isotope budget of the modern ocean: Constraints from riverine magnesium isotope ratios. Earth Planet. Sci. Lett. 250, 241–253. https://doi.org/10.1016/j.epsl.2006.07.037

Wilkinson, B.H., Algeo, T.J., 1989. Sedimentary carbonate record of calcium-magnesium cycling. Am. J. Sci. 289, 1158–1194. https://doi.org/10.2475/ajs.289.10.1158

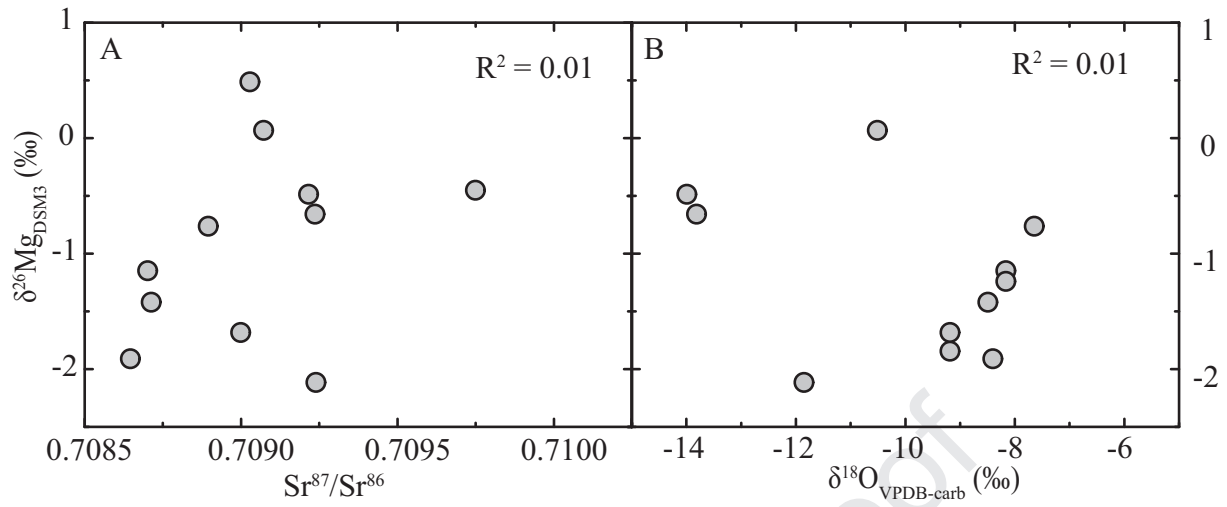Wilson, M.B., 1989. Igneous Petrogenesis. A Global Tectonic Approach. Springer Netherlands.

Wimpenny, J., Yin, Q.Z., Tollstrup, D., Xie, L.W., Sun, J., 2014. Using Mg isotope ratios to trace Cenozoic weathering changes: A case study from the Chinese Loess Plateau. Chem. Geol. 376, 31–43. https://doi.org/10.1016/j.chemgeo.2014.03.008
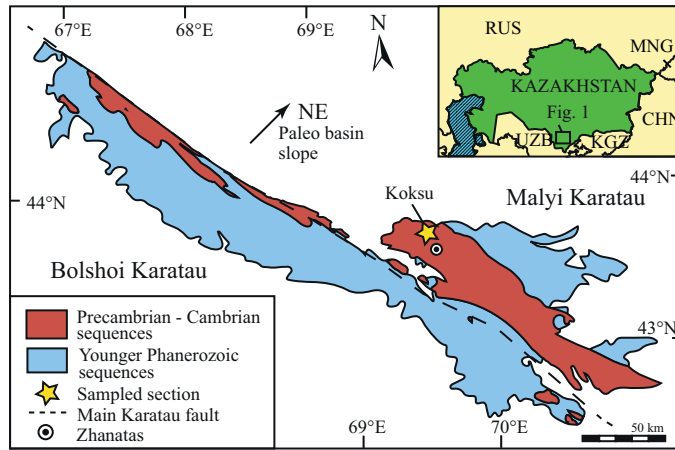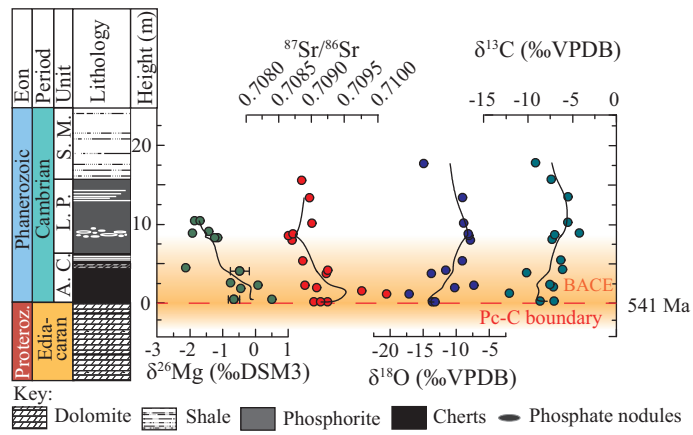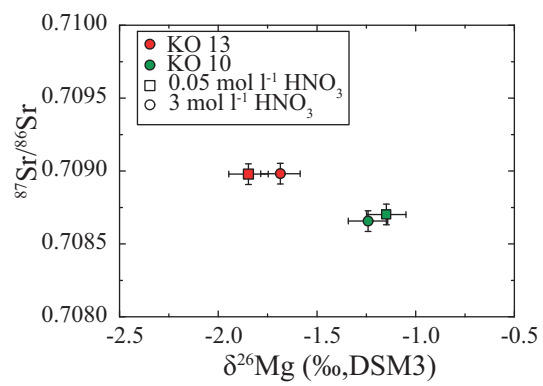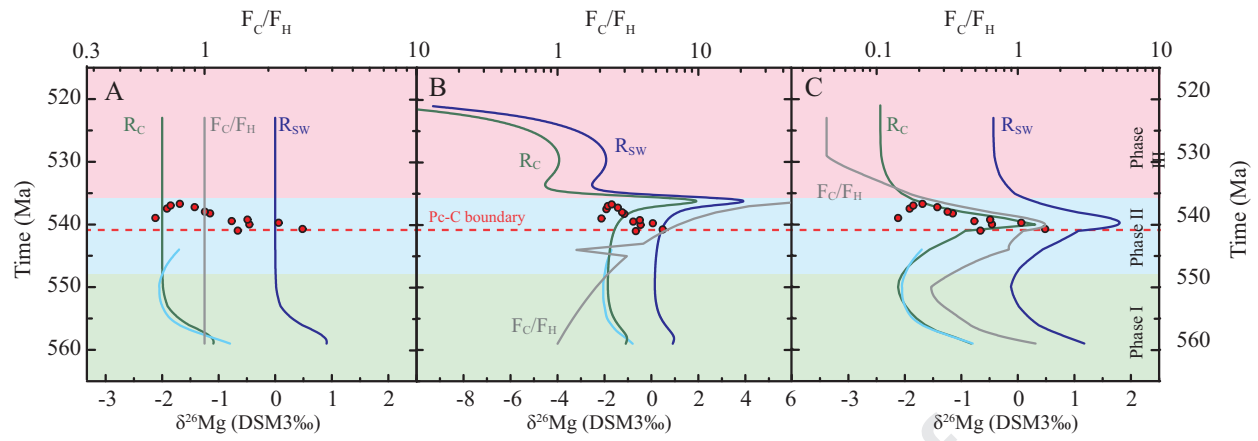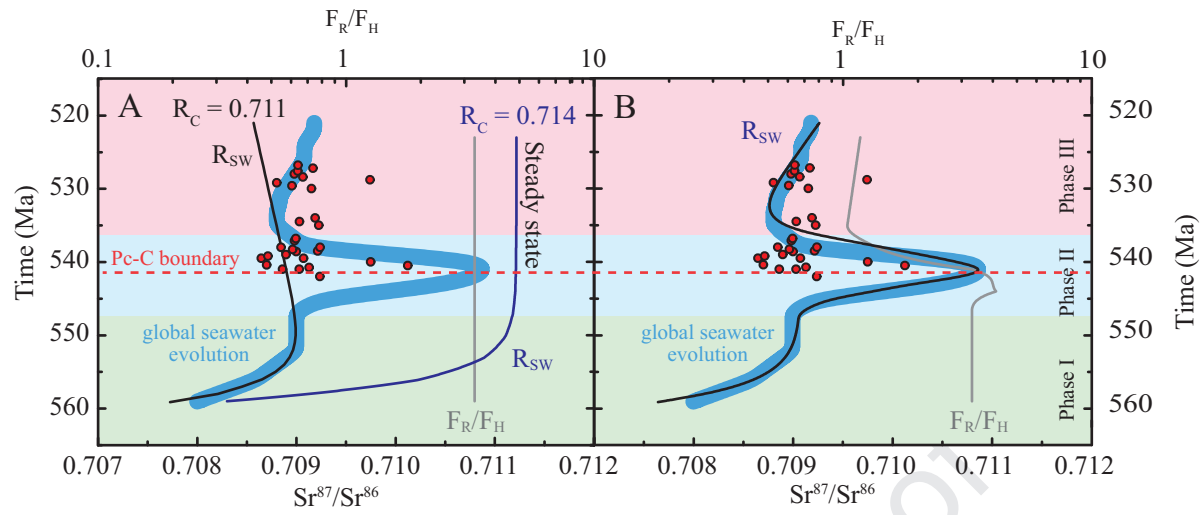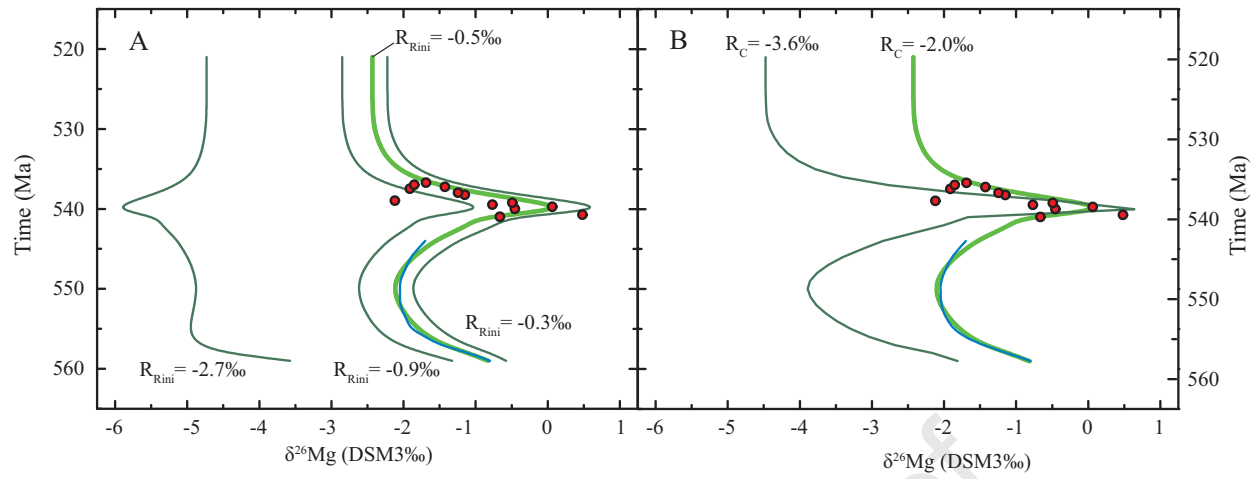
Mg isotopes as a tool for palaeoenvironmental reconstruction in ancient sediments.

Enhanced crustal reworking was a driving force for the Cambrian Explosion.

Sharp positive excursion in seawater δ^{26}Mg at the Precambrian-Cambrian transition.

Dynamic-state model of seawater ^{87}Sr/^{86}Sr and ^{26}Mg.

Conflict of Interest

The authors declare no conflict of interest.